Flower-Shaped Tungsten Oxide with Inorganic Fullerene-like Structure: Synthesis and Characterization

Charlene Ng,[†] Changhui Ye,[‡] Yun Hau Ng,[†] and Rose Amal*,[†]

[†]*ARC Centre of Excellence for Functional Nanomaterials, School of Chemical Engineering, The University of New South Wales, Sydney, New South Wales 2052, Australia, and* [‡]*Key Laboratory of Materials Physics, Institute of Solid State Physics, Chinese Academy of Sciences, Hefei 230031, China*

ABSTRACT: Relatively thick (1.2 μm), novel, flower-like nanostructured tungsten oxide thin films are obtained by electrochemically anodizing tungsten foil in a fluoride containing acidified electrolyte solution. X-ray diffraction analysis reveals the presence of monoclinic hydrated tungstite ($WO_3 \cdot 2H_2O$) in the as-prepared samples, while films annealed at 400 °C for 4 h contain predominantly orthorhombic WO_3 phase. Scanning electron microscopy, transmission electron microscopy, X-ray diffraction, Raman spectroscopy, and UV−vis spectroscopy are utilized to determine the surface morphology, crystal structure, and optical properties of these WO_3 films. An inorganic fullerene-like $WO_3 \cdot 2H_2O$ structure is observed, with the water molecules acting as the coordination solvent and allowing crystallographically specific growth of crystallized $WO_3 \cdot 2H_2O$ through oriented attachment. We propose here that the formation of the flower-like structured hydrated tungstite film occurs through an anodization/precipitation−recrystallization process. The photocurrent measurements under visible light illumination show that the flower-like structure with enhanced surface area exhibits a higher photocurrent density of 0.28 mA cm^{-2}, compared to a photocurrent density of 0.16 mA cm^{-2} obtained for the mesoporous structure. The possibility of controlling and adjusting the morphology by tuning the anodization conditions makes the technique an interesting candidate for fabricating photodevices over a large substrate area.

Introduction

With the ability to extend further into the visible region of the spectrum, tungsten trioxide (WO_3) is an n-type indirect band gap semiconductor with interesting optical, electrical, and structural properties, demonstrating the potential use of these materials in various applications such as electrochromism,[1,2] photocatalysis,[3,4] gas sensing,[5,6] and water splitting.[7] Nanostructured WO_3 is undeniably essential to provide an enhanced surface area and high surface-to-volume ratio for fabrication of such devices that are capable of exhibiting high efficiencies and improved photoresponse, due to the unique properties and superior characteristics of nanodimensional materials.[3,8]

WO_3 possesses a lower band gap energy level of between 2.4 and 2.8 eV as compared to TiO_2, which is currently the most widely studied material for various applications related to photochemical processes. However, pure WO_3 has a lower light-to-energy conversion efficiency than TiO_2 as the reduction potential of electrons in WO_3 is low due to its low conduction band level.[9] There are two proposed approaches that can be employed to improve photoresponse and light conversion efficiency of WO_3. The first approach is doping the material with nanometal particles such as platinum, which are able to trap photogenerated electrons and enhance the photoresponse of WO_3.[10] The second approach is controlling the synthesis process of WO_3, as the photoresponse properties are closely related to the particle dimension and morphology of the material.[11,12]

Among the various methods developed to synthesize nanostructured WO_3 thin films, such as chemical vapor deposition, physical vapor deposition, and sol−gel techniques, electrochemical anodization of tungsten metal in fluoride containing electrolytes is one of the simplest processes to produce nanostructures on a large area substrate, with a high surface to volume ratio and enhanced electro-optical properties.[13] The surface morphology of nanostructured WO_3 prepared by the anodization method can be easily tuned by altering the anodization potential, duration, electrolyte solution, temperature, and other physical conditions that constitute the anodization process. The preparation of self-organized nanoporous WO_3 thin films by anodization of tungsten foil in NaF electrolytes was reported by Schmuki et al.,[14] while Sadek et al.[15] recently reported the fabrication of WO_3 nanoplatelets by the anodization of tungsten foil at high temperatures in a nitric acid environment. This strongly suggests that controlling the synthesis conditions can significantly influence the morphology of the resulting WO_3 thin film, fabricated by the anodization process. However, the main limitation of this technique lies in the thickness of the film produced,[16] as a result of a steady state being reached rapidly during the anodization process.[15] On average, less than 600 nm films were obtained using the anodization technique, which is less than the ideal for the various photoresponse applications.[17,18]

In this work, we aim to synthesize relatively thicker nanostructured WO_3 thin films with improved photoresponse and light conversion efficiency using the anodization process. The formation mechanism and the physicochemical and optical properties of the flower-like structured tungsten oxide film will be investigated through extensive characterization studies, including scanning electron microscopy (SEM), transmission electron microscopy (TEM), X-ray diffraction (XRD), Raman spectroscopy, and UV−vis spectroscopy. The photoresponse of these films under visible light illumination will also be performed.

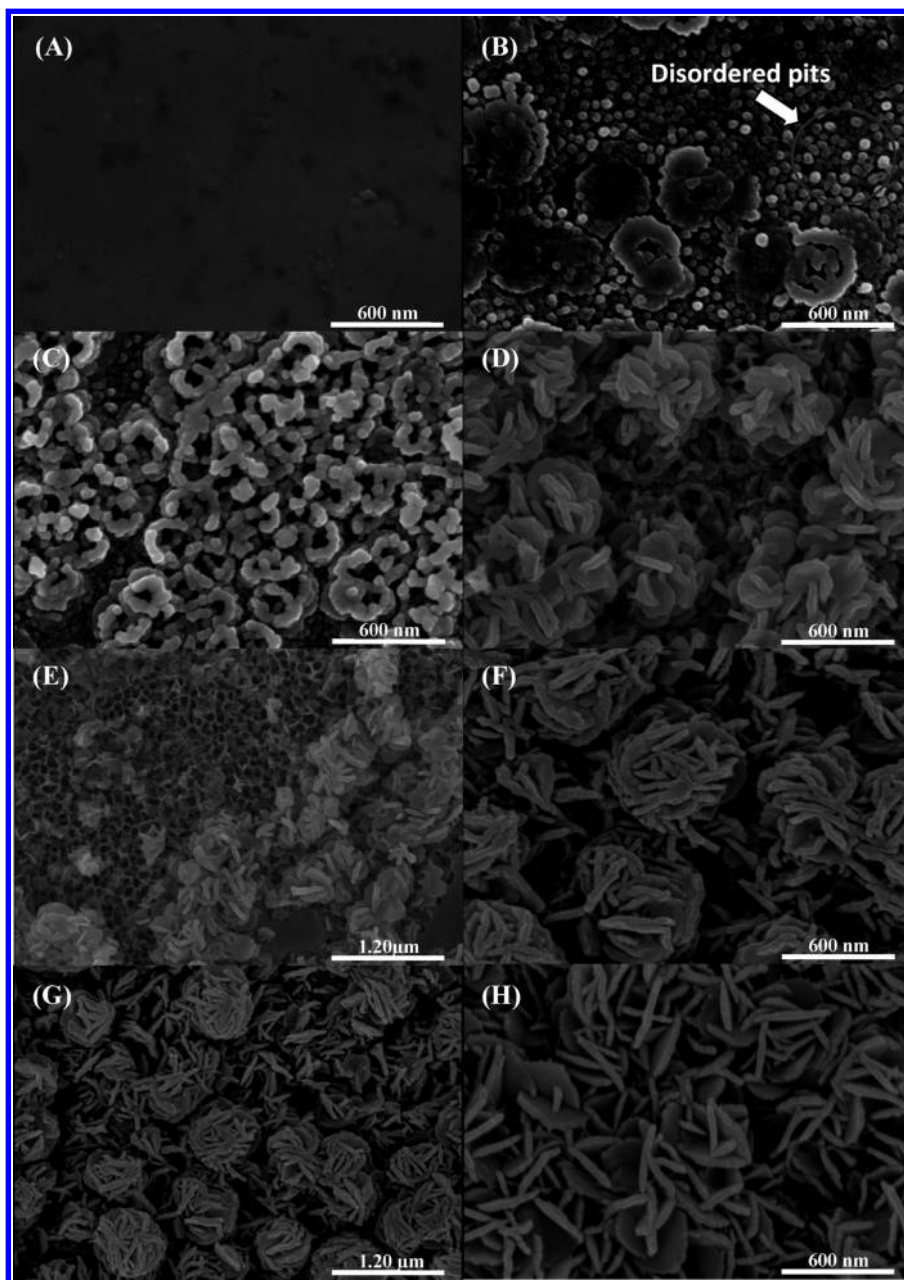*To whom correspondence should be addressed. E-mail: r.amal@ unsw.edu.au.

Figure 1. SEM images of W foil after different anodization duration at an applied potential of 50 V is taken to investigate the growth of nanostructured WO_3. W foil anodized for (A) 0 min, (B) 10 min, (C) 20 min, (D) 40 min, (E) 40 min (illustrating that some parts contain porous structures), (F) 60 min, (G) 60 min (at a lower magnification of 25 K), and (H) 60 min (calcined at 400 °C for 4 h), respectively.

Experimental Details

Tungsten (W) foil (Alfa Aesar, 99.95%, 0.05 mm thick) were anodized in 120 mL of electrolyte solution consisting of 1 M sulphuric acid (H_2SO_4, Univar, 98%) and 0.5 wt % sodium fluoride (NaF, Analar, 99%). Prior to the electrochemical anodization process, the tungsten foils were degreased by sonicating in acetone and followed by deionized water. The samples were then contacted with a Cu spring and pressed against an O-ring in an anodization cell, leaving 4.15 cm^2 exposed to the electrolyte solution. The anodization cell consists of a two-electrode configuration with a platinum foil as the counter electrode (cathode) and the tungsten foil as the working electrode (anode); the distance between the cathode and the anode was kept constantly at 2 cm. All experiments were performed in static conditions, unless otherwise stated. For anodization we employed a Delta Elektronika Power Supply D 050-10, and the voltage was held at a selected voltage for different periods. The anodized samples were then properly washed with deionized water and air-dried.

Subsequently, thermal treatment of the WO_3 films was carried out at 400 °C for 4 h with a ramping rate of 2 °C/min in air environment. The samples were then allowed to cool down by natural convection in the furnace back to ambient condition.

A scanning electron microscope (SEM, Hitachi S4500, operating accelerating voltage of 10 kV) was used to analyze the morphology of the WO_3 nanostructures. Transmission electron microscopy (TEM, Philips CM200) analysis was carried out by scratching a portion of the WO_3 film, followed by ultrasonication in ethanol solution for 10 min for proper dispersion. A drop of the sonicated sample was placed on the carbon coated Cu grid and subjected to TEM analysis. Glazing angle X-ray diffraction analysis was employed for the characterization of the crystalline structure of the samples. Measurements were collected at room temperature using Cu Kα radiation (λ = 1.54 Å) with a potential of 40 kV and a current of 30 mA. Micro-Raman measurements were performed with a Renishaw inVia spectrometer utilizing a 514 nm wavelength of Argon ion laser with 1800 lines/mm grating. Diffuse reflectance ultraviolet and visible (DRUV−vis)

spectra of the films were recorded in a range of 200−800 nm to investigate the light harvesting properties of WO_3 thin films using a UV−vis spectrophotometer (Cary 5 UV−vis-NIR). The reflectance of the sample was measured and the corresponding absorbance (F(R)) was calculated using the Kubelka−Munk theory. The optical band gap value is defined by the intercept of the plot of $(F(R)h\nu)^{1/2}$ against $h\nu$, where $F(R)$ and $h\nu$ denote the absorbance and photon energy, respectively. Photocurrent measurements of the samples were taken in 0.5 M H_2SO_4 at room temperature using Autolab potentiostat/galvanostat (model PGSTAT302N) at 1.5 V in a standard three-electrode configuration with platinum wire as counter electrode, Ag/AgCl as the reference electrode, and WO_3 film as the working electrode under visible light illumination (420 nm). Nitrogen gas was also constantly bubbled in the system for the entire duration of photocurrent measurements.

Results and Discussion

The growth of the tungsten oxide structures was monitored by taking SEM images after different anodization time intervals at an applied potential of 50 V as illustrated in Figure 1. Before anodization, no visible structure was observed on the tungsten foil (Figure 1A). After 10 min of anodization, nanostructures appeared with disordered pits, as shown in Figure 1B. These seemed to be the sites of initial pore growth, while the patches of oxide layer were reflected as the initial precipitation and overgrowth of the oxide layer. As the anodization time increases to 20 min (Figure 1C), porous structure with a pore diameter of approximately 60 nm developed and a decrease in disordered pits coverage area was also observed. Mixtures of nanoporous structures (Figure 1E) with a pore diameter of approximately 75 nm and flower-like structures (Figure 1D) with a platelet thickness of approximately 25 nm were clearly visible after an anodization time of 40 min. This observation indicated that the flower-like structures only started to form after 40 min of anodization and the formation only occurs after the anodic growth of the porous oxide layer. This suggests that the growth of these flower-like structures require soluble species that are generated by the initial anodic growth of the oxide layer. Consequently, the oxide layer continued to grow into spheres of flower-like structures with a platelets thickness of approximately 42 nm. No nanoporous structures could be observed after an anodization time of 60 min (Figure 1F,G). After calcination, the flower-like structures appeared to be more crystalline and started to unwrap, thus revealing the petals that exhibited a similar thickness of approximately 45 nm (Figure 1H). The change in the structure might be due to the change in crystalline structure and chemical species, which will be further discussed in this paper.

In our experiments, the nanostructured thin films with flower-structured morphology were prepared by the anodization method using acidified fluoride containing electrolyte (pH = 0.8) at room temperature. We found that the thin films of the flower-like structures could be obtained by establishing a supersaturation condition within the anodization cell, whereby sparingly soluble products were concentrated at the bottom of the cell due to the applied electric field. In contrast, when stirring was introduced, the soluble products were evenly distributed and therefore a supersaturated condition could not be achieved, leading to the formation of porous structures (Figure 2) with a film thickness of approximately 600 nm.[18] Figure 1G illustrates the SEM images of the resulting flower-structured thin film anodized at 50 V for 60 min and the thickness of the flower platelets were on the order of 40−50 nm, with a film thickness of approximately 1.2 μm.[18] We also observed that the nanoplatelets, which are mostly aligned normal
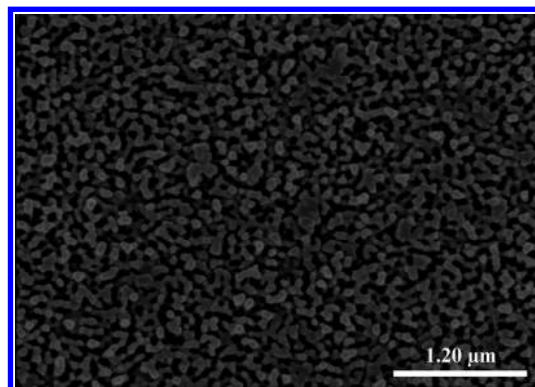

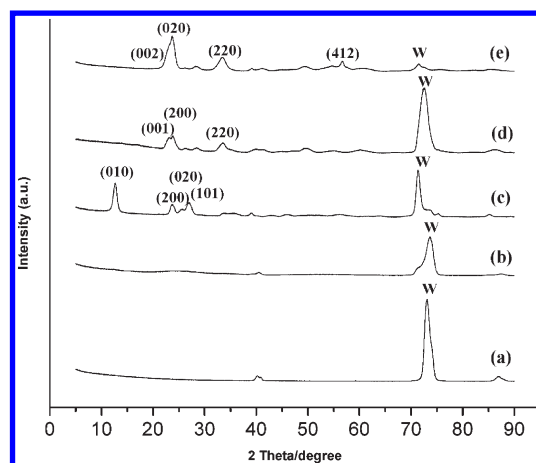**Figure 2.** SEM image of nanoporous WO_3 thin film when stirring was introduced.

Figure 3. XRD analysis of (a) tungsten foil, (b) WO_3 porous film (with stirring) before calcination, (c) as-anodized flower-structured WO_3 after 60 min anodization, (d) WO_3 porous film (with stirring) annealed at 400 °C for 4 h, and (e) flower-structured WO_3 after 60 min anodization and annealed at 400 °C for 4 h. The tungsten foil and porous structure are found to be amorphous with peaks arising solely from the tungsten substrate (labeled as "W"). The as-anodized WO_3 thin film is found to be monoclinic $WO_3 \cdot 2H_2O$ and converted to orthorhombic WO_3 after calcination.
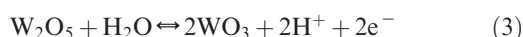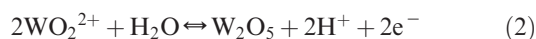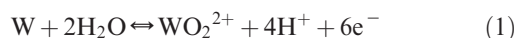
to the substrate surface, intertwined intensively with each other to form spheres of flower-like structures, indicating a minimization process of the surface. The meso/macrodimensional gaps observed between the structures are able to provide high porosity, which is essential to achieve good efficiencies in most surface-sensitive devices. Amano et al.[16] have also observed similar WO_3 morphology through a wet chemical synthesis involving sol−gel and a newly developed solvothermal method. They reported an enhancement of PEC efficiency possibly due to the relatively low density of grain boundaries in the path of electron transport and high photoabsorption ability and large surface area,[16] therefore suggesting the potential of this flower-like WO_3 morphology in enhancing the performance of photodevices.

Figure 3 shows the XRD patterns of the W substrate, porous film (with stirring) before and after calcination and the flower-structured WO_3 film before and after calcination. The peaks have been indexed to the tungsten oxide structures, with peaks arising from the tungsten substrate labeled as "W". It is evident that the porous film displays only peaks from the W substrate and is therefore revealed to be completely amorphous, as reported by various authors.[2,18] The most stable

WO$_3$ phase at room temperature exhibits a monoclinic structure, and this phase is further transformed to orthorhombic at 330 °C and is stable up to 740 °C.[19-21] X-ray diffraction analysis revealed the presence of monoclinic hydrated tungstite (WO$_3$·2H$_2$O), with the highest peak indexed to the (010) plane in the as-prepared samples, while films annealed at 400 °C (maintained at 4 h) with a 2 °C/min upward and downward ramping contained predominantly the orthorhombic WO$_3$ phase. The hydrated tungstite experienced a loss of water after calcination, as confirmed by the presence of two characteristic peaks at 22.7° and 23.6° corresponding to (002) and (020) planes and the disappearance of a strong intensity peak at 13.0° corresponding to the (010) plane in the XRD pattern. A similar observation is reported by Sadek et al.[15] whereby the monoclinic hydrated tungstite was transformed to orthorhombic WO$_3$ after the annealing treatment at 400 °C for 4 h. Judeinstein et al.[22] also concluded that the irreversible thermal dehydration of hydrated tungstite and crystallization occurs at 350 °C, leading to orthorhombic WO$_3$. Similarly, the porous film after calcination at 400 °C (maintained at 4 h) also exhibits an orthorhombic WO$_3$ structure with the highest peak indexed to the (200) plane.

From the above observations, we believe that the mechanism of anodic growth of the flower-structured oxide layer on the tungsten surface is governed by (i) the anodic oxide formation, (ii) chemical dissolution of the oxide layer, and (iii) successive precipitation of sparingly soluble products (WO$_3$·2H$_2$O) on the surface, causing thickening of the porous films (Scheme 1).

The initial anodic growth of oxide layer is an electrochemical process, as shown in Scheme 1, according to the following reactions:[23]

$$W + 2H_2O \leftrightarrow WO_2^{2+} + 4H^+ + 6e^- \qquad (1)$$

$$2WO_2^{2+} + H_2O \leftrightarrow W_2O_5 + 2H^+ + 2e^- \qquad (2)$$

$$W_2O_5 + H_2O \leftrightarrow 2WO_3 + 2H^+ + 2e^- \qquad (3)$$

Reaction 1 describes the oxide growth on tungsten in a fluoride-free electrolyte, whereby O^{2-} ions from the H$_2$O react with the oxidized tungsten (W^{4+}) to form an oxide layer of WO$_2^{2+}$ on the surface. Subsequently, WO$_2^{2+}$ will be attacked by water to form W$_2$O$_5$ intermediate as shown in reaction 2. Since WO$_2^{2+}$ and W$_2$O$_5$ are intermediates that decompose in the presence of water at 25 °C, hexavalent WO$_3$ which is stable in this condition will be formed (Reaction 3) on the film eventually.[23] Further oxide growth is controlled by the field-enhanced ion transport (W^{4+} and O^{2-}) through the growing oxide. This process is self-limiting under a constant applied voltage, as the field within the oxide layer is progressively reduced by the increasing oxide thickness, thus resulting in the growth of a compact WO$_3$ film with finite thickness.[24]

Alternatively, nanoporous films of WO$_3$ can be achieved in the presence of fluoride ions in the electrolyte solution. This is due to the ability of tungsten to form soluble fluoride complexes. Disordered pits are initiated and a nanoporous structure is subsequently developed by the chemical dissolution of the oxide layer or the direct complexation of high-field transported W^{4+} at the oxide electrolyte interface to form soluble fluoride complexes.[24]

The anodic growth of the WO$_3$ porous oxide layer becomes a competition between the anodic tungsten oxide formation and the chemical dissolution of the tungsten oxide layer in a

Scheme 1. Schematic Illustration of the Formation Process of Flower-Structured WO$_3$ Thin Film[a]
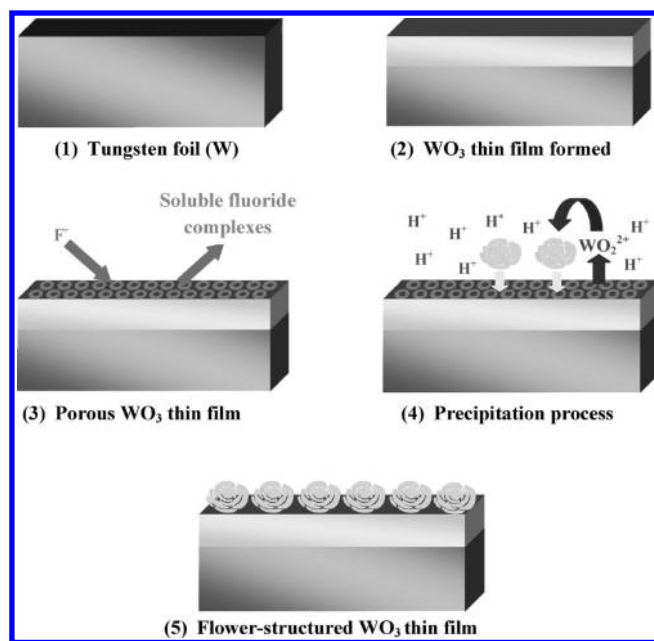
[a] (1) Tungsten foil as the starting material and substrate. (2) Compact WO$_3$ film growth. (3) Nanoporous structure formed in the presence of fluoride ions (F$^-$) to form soluble fluoride complexes. (4) WO$_2^{2+}$ is generated due to the low pH and supersaturation condition and leads to the precipitation and growth of sparingly soluble products (WO$_3$·2H$_2$O) as represented by the light gray particle. (5) Flower-structured WO$_3$ thin film formed as a result of anodic growth of oxide later and the successive precipitation and crystal growth process.

fluoride containing electrolyte solution.[2] During the anodization process, the continual growth of the tungsten oxide layer and chemical dissolution of the tungsten oxide layer occurs simultaneously and a steady state is established when the growth rate at the metal−metal oxide interface is the same as the dissolution rate of oxide film at the outer interface.[3,13,14,24] However, for tungsten, the steady state between these two competing processes is reached rapidly during the anodization process, consequently limiting the thickness of the porous WO$_3$ film produced.

At low pH (pH < 1), there are two possible simultaneous dissolution processes that could proceed after the initial anodic growth of the oxide layer, according to the following reactions:[25]

$$W + 2H_2O \leftrightarrow WO_2^{2+} + 4H^+ + 6e^- \qquad (1)$$

$$WO_3 + 2H^+ \leftrightarrow WO_2^{2+} + 2H_2O \qquad (4)$$
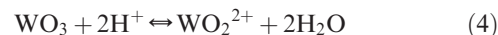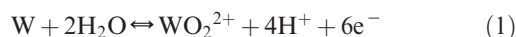
Reaction 1 is the electrochemical dissolution through the oxide and favored by the electric field, while reaction 4 is the chemical dissolution of the oxide layer (WO$_3$) formed. El-Basiouney et al. also concluded that the dissolution of WO$_3$ in acidic medium takes place via the formation of WO$_2^{2+}$ species, which is consistent with the above-proposed mechanism.[26] The possibility of generating WO$_2^{2+}$ at low pH could lead to the precipitation of primary particle nuclei induced by the supersaturation condition and crystal growth of the soluble products on the film surface, causing thickening of the WO$_3$ nanostructured film.[23] Therefore, the precipitation and growth process are driven by the supersaturation condition established within the anodization cell, the instability of WO$_2^{2+}$ in the presence of water at room temperature, and the presence of a
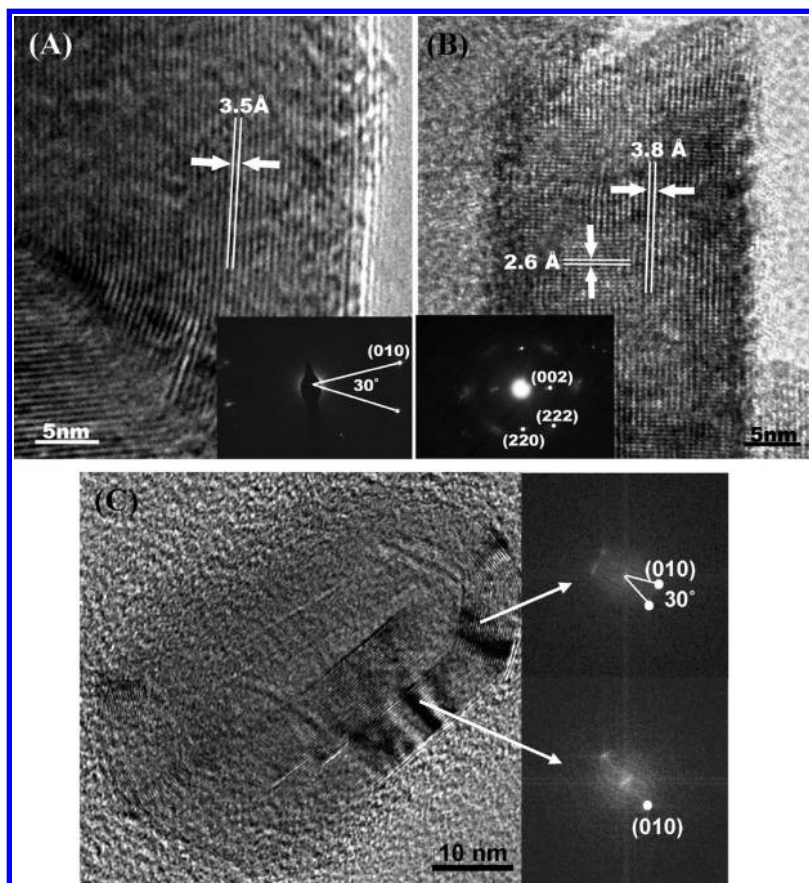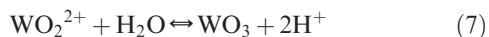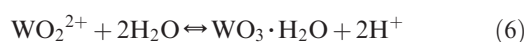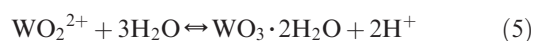
Figure 4. TEM images of flower-structured WO_3 (A) before and (B) after calcination. The insets are the selected area electron diffraction (SAED) patterns of the WO_3 depicting the corresponding lattice planes of the material (C) FFT pattern taken at two different positions of the sample to illustrate the existence of two spots positioned at 30° away from each other.

high electric field at the oxide−solution interface, which can be described by the following reactions:

$$WO_2{}^{2+} + 3H_2O \leftrightarrow WO_3 \cdot 2H_2O + 2H^+ \quad (5)$$

$$WO_2{}^{2+} + 2H_2O \leftrightarrow WO_3 \cdot H_2O + 2H^+ \quad (6)$$

$$WO_2{}^{2+} + H_2O \leftrightarrow WO_3 + 2H^+ \quad (7)$$

The involvement of soluble species in the dissolution−precipitation mechanism is demonstrated as different structures of WO_3 films are obtained by the introduction and absence of stirring during the anodization process. This is expected as stirring reduces the concentration of soluble species ($WO_2{}^{2+}$) close to the surface, causing the precipitation and recrystallization process of the sparingly soluble products to be hindered and the growth rate to decrease drastically.[27] Therefore, amorphous porous WO_3 (Figure 2) results when stirring is introduced. In contrast, the flower-structured WO_3, observed from the SEM images (Figure 1) formed, is essentially the product of a combined effort of anodic growth of the oxide layer in fluoride containing electrolyte, and the successive precipitation and crystal growth of the primary particle nuclei induced by the supersaturation condition. The presence of fluoride ions, which leads to the formation of a porous structure, is important to generate soluble ions for the formation of the flower-like structure. The supersaturation degree of these soluble species thus dictates the growth mechanism of the flower-like structure, as the controlled synthesis of polycrystalline

platelets often involves the nucleation of primary particles induced by the supersaturation condition followed by their aggregation. At exceptionally high supersaturation conditions, the nucleation of tungsten oxide species is expected to occur randomly in the electrolyte solution by homogeneous crystallization, resulting in the formation of polycrystalline flower-like platelets composed of randomly oriented primary nanocrystallites with different domains oriented in various orientations through a mechanism known as random aggregation. At lower supersaturation, an oriented attachment whereby primary particles coalescing with one another in a highly oriented fashion that involves spontaneous self-organization is expected to occur during the anodization process.[28] We expect secondary particles exhibiting new single crystals (inorganic fullerene-like structures) to be produced, with water present in the electrolyte solution acting as the coordination solvent.[29] This results in the growth of an inorganic fullerene-like $WO_3 \cdot 2H_2O$ structure (Figure 4C) in the as-anodized samples due to the layered crystallography nature of $WO_3 \cdot 2H_2O$.[28] Inorganic fullerene-like structures are usually formed when the total surface energy is to be minimized, while the strain energy is simultaneously generated. Therefore, only in rare cases, and under optimized conditions, could the inorganic fullerene-like structures be formed. We report here for the first time that anodization/precipitation−recrystallization processes could achieve this unique structure. The subsequent precipitation and recrystallization process at low pH conditions is the most significant means of achieving thicker WO_3 flower-structured films, as the thickness of the
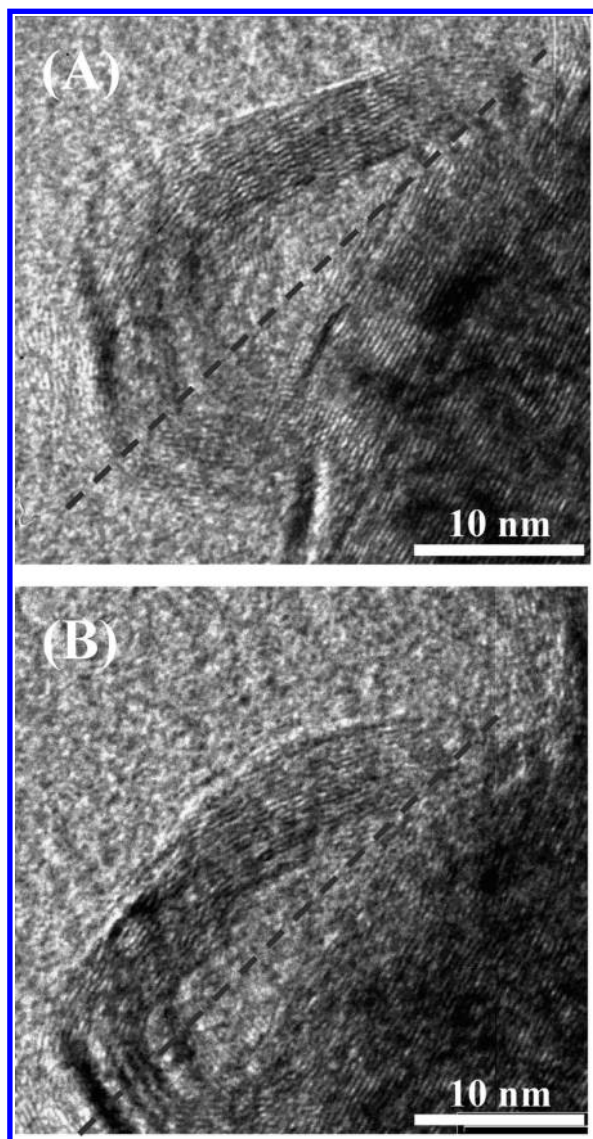
Figure 5. TEM images of sample before calcination, showing the preservation of symmetry of the layered structure (A) before and (B) after the sample holder was tilted 15° during TEM characterization. The dotted lines represent the line of symmetry of the sample.

anodized porous films is often limited by the rapidness of the steady state reached between the two competing processes as mentioned previously.

Since crystallization is closely related to the formation of solid crystals precipitating from a solution, the proposed complex dissolution−precipitation mechanism is confirmed by the presence of a monoclinic crystal structure in the as-anodized sample. XRD analysis also verified that the precipitation process follows predominantly Reaction 5, thus suggesting that the high water content in the electrolyte solution essentially favors the precipitation of $WO_3 \cdot 2H_2O$ onto the surface of the film.

The transition of monoclinic hydrated tungstite to orthorhombic WO_3 is also investigated by analyzing the TEM images taken before and after calcination as shown in parts A and B of Figure 4, respectively. Without annealing, the lattice spacing of 3.5 Å between the adjacent fringes corresponds to the *d*-spacing of (010) planes of the monoclinic $WO_3 \cdot 2H_2O$. The selected area electron diffraction (SAED) pattern shown in the inset of Figure 4A is indexed to the

presence of the (010) plane. Interestingly, nanosheets that are being coiled and bent in a circular manner can be observed in Figure 4C. This is primarily due to the ability of $WO_3 \cdot 2H_2O$ to form sheets of layered structures with water molecules intercalated between the oxide planes.[22,30] The position of the intercalated water molecules are represented by the small circles as illustrated in the structural schematic representation of $WO_3 \cdot 2H_2O$ (Figure 6A). These water molecules are located in between the oxide planes, possibly forming intermolecular attractions such as van der Waals forces, dipole−dipole attractions, and hydrogen bonding with the adjacent oxide layer, thus resulting in a layered structure. Similarly, the spot located at 30° away from the (010) plane could also be indexed to the (010) plane. The existence of this atypical spot is mainly due to the bending of the lattice fringes, which results in a similar (010) spot diffracted at an angle away from each other. This phenomenon is clearly depicted by the demonstration of fast Fourier transform (FFT) and the corresponding diffraction pattern taken at different positions of the sample shown in the insets of Figure 4C.

The symmetry of the layered structure is also preserved when the sample holder was tilted 15° during the TEM characterization as shown in Figure 5. The preservation of lattice images emphasized the presence of a polyhedral structure (Figure 4C) in $WO_3 \cdot 2H_2O$ that is closed in three dimensions, which further verifies the presence of an inorganic fullerene structure as discussed previously.[31] The closure of $WO_3 \cdot 2H_2O$ sheets into a more compact structure is due to the minimization of surface energy by the elimination of dangling bonds at the edges as elucidated from the energetic point of view. Alternatively, the mechanism for growth of these structures may also involve solvent molecules, whereby strain of the layers is reduced or eliminated by solvent molecules such as oxide formation at the bends.[31]

From the TEM image in Figure 4B, the lattice fringes can be clearly observed, indicating improved crystallinity of the sample after annealing. The lattice spacing of 3.9 Å and 2.6 Å between the adjacent fringes corresponds to the *d*-spacing of (002) and (220) planes of the orthorhombic WO_3 imaged along a zone axis of [1$\bar{1}$0]. Ideally, the oxide layer would bind to the adjacent oxide layer following the removal of water molecules through calcination and be able to retain the pre-existing monoclinic structure. Instead, orthorhombic WO_3 was formed after the anneal treatment at 400 °C. The structural schematic representation of WO_3 shown in Figure 6B reflects an increase in the dimensions of the unit cell after calcination. This indicates that the thermal treatment essentially provides energy for the atoms to rearrange and the ability to achieve the most stable form of WO_3 crystal structure (orthorhombic) at 400 °C.

The change in optical properties of the WO_3 films as the anodization duration increases and after anneal treatment can be observed by the absorption studies and the corresponding optical band gap energy shown in Figure 7. As the anodization time increases from 10 to 60 min, the absorption edges of the WO_3 films (Figure 7A) shifted significantly from 378 to 400 nm, extending more into the visible spectrum as the oxide layer grows. The absorbance values at higher wavelengths can be contributed by the presence of oxygen vacancies on the film. As the anodization time increases, the amount of suboxides and oxygen vacancies decreases and hence the absorbance values decrease with anodization time. After calcination, the absorption edge of the film is further shifted to 428 nm, illustrating its enhanced ability of extending more into the visible wavelength range with improved crystallinity.
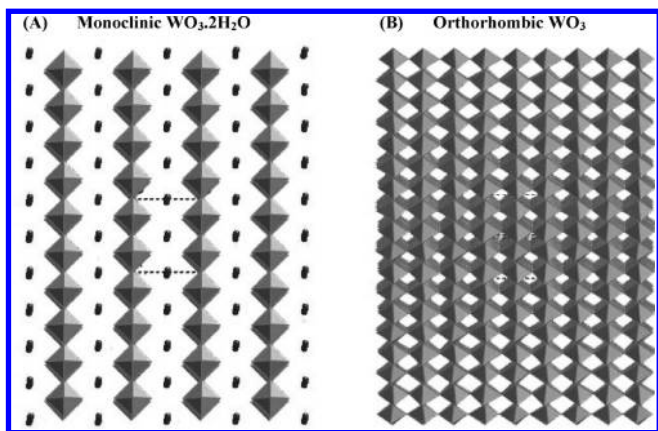
Figure 6. Schematic representation of (A) monoclinic $WO_3 \cdot H_2O$ and (B) orthorhombic WO_3. The positions of the intercalated water molecules are represented by the small circles as illustrated in the structural schematic representation of $WO_3 \cdot 2H_2O$ in (A).

Figure 8. Raman spectra of WO_3 samples prepared at different anodization times and after annealing. The tungsten foil is treated as the reference sample.
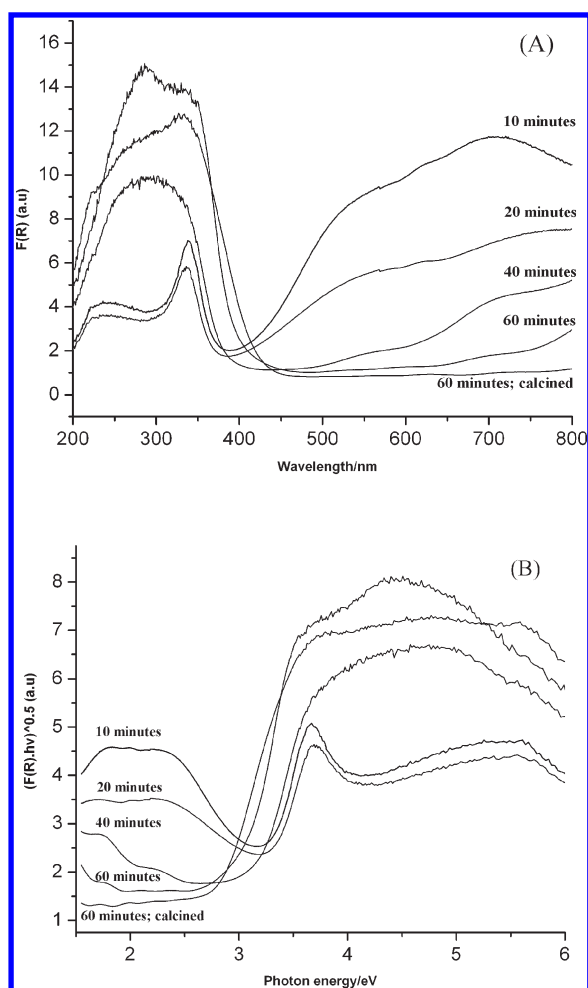

Figure 7. (A) Absorption spectra and (B) optical band gap spectra of the tungsten oxide thin films at different anodization times and after annealing.

WO_3 is an indirect band gap semiconductor and the optical band gap of these films can be determined by considering the indirect transition between 2p electrons from the valence band of oxygen and the 5d conduction bands of tungsten as defined by the Tauc's plot.[3,32] From Figure 7B, the band gap energies of the WO_3 films dropped from 3.1 to 2.8 eV as the anodization time increases from 10 to 60 min. These values were in
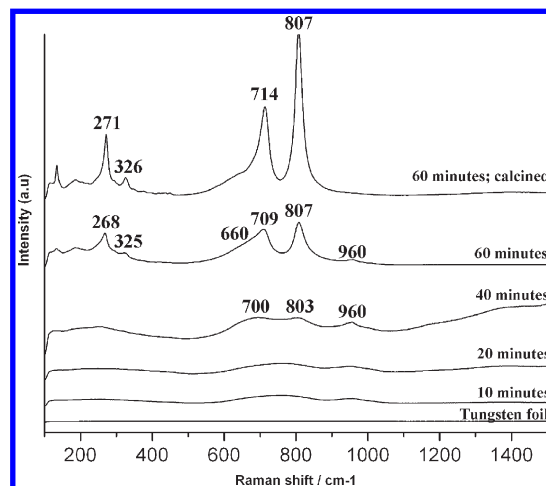
accordance with the literature, whereby band gap values of approximately 3.2 eV were reported for amorphous WO_3, while monoclinic crystalline structure showed typical values of around 2.6 eV.[18,33] Similarly, the optical band gap energy is further reduced and resulted as 2.6 eV with improved crystallinity after calcination.

In Raman spectra, there are three frequency regions that can be individuated for tungsten oxide crystalline phases. The first region occurs at very low frequencies, where several peaks related to the lattice modes such as relative translational or rotational motions of the WO_6 octahedral units in the same unit cell appear. The second region occurs at intermediate frequencies of $200-400$ cm^{-1}, reflecting the O−W−O bending mode. The last region occurs at high frequencies ($600-900$ cm^{-1}) with peaks linked to the O−W−O stretching modes.[34]

Raman spectra of the samples investigated are shown in Figure 8. No Raman signal was identified for the tungsten foil (starting material). Subsequently, bands start to evolve which indicates the formation of the oxide layer as the anodization time increases from 10 to 60 min. Some intense peaks at characteristic frequencies of crystalline WO_3 structure were also observed after 60 min of anodization. The peaks observed at 709 and 807 cm^{-1} can be attributed to the stretching modes arising from W−O, while the lower frequency bands of 268 and 325 cm^{-1} can be assigned to the W−O−W bending vibrations.[30,35] The low intensity band occurring at 960 cm^{-1} is a spectral marker for amorphous material. It is contributed by the symmetric stretching mode of terminal W=O bond, and it represents the lattice discontinuities at terminal W=O for the anodized samples before annealing. The broad spectrum at 660 cm^{-1} can be attributed to the hydration level of the crystal.[15] A doublet at 660 and 680 cm^{-1} that can be identified as $WO_3 \cdot 2H_2O$ is possibly embedded within the broad shoulder band. The low intensity bands of 700 and 803 cm^{-1} reflect the initial growth of $WO_3 \cdot 2H_2O$, corresponding to the peaks observed at 709 and 807 cm^{-1}.

After thermal annealing at 400 °C, the spectral features of the films changed with Raman bands becoming sharper and exhibiting higher intensities. This evolution and peak sharpening revealed a sign of increasing crystallinity and order after calcination.[34] The terminal W=O stretching mode at 960 cm^{-1} disappeared and the two bands at 714 and 807 cm^{-1}
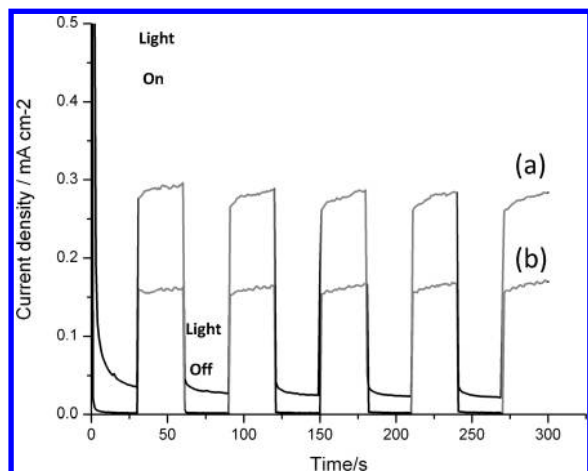
Figure 9. Photocurrent responses of (a) flower-like structure and (b) mesoporous structure of WO_3 thin film under visible light illumination (420 nm) at 1.5 V applied voltage. The switch-on/-off period is 30 s and the electrolyte used is 0.5 M H_2SO_4.

became stronger and sharper. Similarly, the peaks observed at 714 and 807 cm^{-1} can be attributed to the stretching modes arising from W−O, while the lower frequency bands of 271 and 326 cm^{-1} can be assigned to the W−O−W bending vibrations.[30,35]

Photoresponses of WO_3 flower-like structure (Figure 1H) and mesoporous structure thin films (Figure 2) are presented in Figure 9. Under visible light illumination and 1.5 V applied voltage, a photocurrent density of 0.28 mA cm^{-2} was generated by the flower-like structure, whereas only 0.16 mA cm^{-2} was generated by the mesoporous structure under the same conditions. This suggests that the meso/macrodimensional gaps observed in between the flower-like structure and an increase in flower-like film thickness to 1.2 μm from 600 nm thickness are able to provide high porosity and enhanced surface area exposed to the electrolyte. The interconnected platelets are also capable of exhibiting improved electron transfer, hence producing higher photocurrent as compared to the mesoporous structure. Furthermore, the light trapping effect caused by the internal reflection of incoming irradiation on the platelets positioned at an angle with adjacent platelets could also contribute to the significant increase in photocurrent generated by the flower-like structure.

Conclusion

In summary, we have described a low cost and simple method to produce flower-structured nanocrystalline thin films of tungsten oxide and characterized these films using SEM, TEM, XRD, UV−vis, and Raman to determine the morphology, crystal structure, and optical properties. The resultant flower-structured tungsten oxide film is the product of anodic growth of oxide layer in fluoride containing electrolyte and the successive precipitation induced by the supersaturation condition and growth of the sparingly soluble products ($WO_3 \cdot 2H_2O$) at low pH conditions within the anodization cell. The $WO_3 \cdot 2H_2O$ exhibits an inorganic fullerene-like structure with layered crystallography. The water molecules of $WO_3 \cdot 2H_2O$ act as the coordination solvent that results in the growth of inorganic fullerene-like structure through oriented aggregation. Analysis of the X-ray diffraction, TEM and Raman results revealed the presence of monoclinic hydrated tungstite ($WO_3 \cdot 2H_2O$) in the as-anodized samples. After annealing at 400 °C for 4 h, the hydrated tungstite ($WO_3 \cdot 2H_2O$) loses the

water molecules and crystalline orthorhombic WO_3 thin film is formed. The flower-like structure with enhanced surface area and thickness exhibits a higher photocurrent density of 0.28 mA cm^{-2} under visible light illumination, compared to the mesoporous structure, which only produces a photocurrent density of 0.16 mA cm^{-2}. The current inexpensive method of producing flower-structured WO_3 thin films with a high surface area may find potential applications in water splitting, dye-sensitized solar cells, and photocatalysis.

References

(1) Baeck, S. H.; Choi, K. S.; Jaramillo, T. F.; Stucky, G. D.; McFarland, E. W. *Adv. Mater.* **2003**, *15*, 1269.
(2) Nah, Y.-C.; Ghicov, A.; Kim, D.; Schmuki, P. *Electrochem. Commun.* **2008**, *10*, 1777.
(3) Guo, Y.; Quan, X.; Lu, N.; Zhao, H.; Chen, S. *Environ. Sci. Technol.* **2007**, *41*, 4422.
(4) Yu, J.; Qi, L. *J. Hazard. Mater.* **2009**, *169*, 221.
(5) Liu, Z.; Yamazaki, T.; Shen, Y.; Kikuta, T.; Nakatani, N. *Sens. Actuators, B* **2007**, *128*, 173–178.
(6) Nimittrakoolchai, O.; Supothina, S. *Mater. Chem. Phys.* **2008**, *112*, 270.
(7) Wang, H.; Lindgren, T.; He, J.; Hagfeldt, A.; Lindquist, S. *J. Phys. Chem. B* **2000**, *104*, 5696.
(8) Fang, X.; Ye, C.; Zhang, L.; Zhang, J.; Zhao, J.; Yan, P. *Small*, *1*, 422.
(9) Zhao, Z. G.; Masahiro, M. *Angew. Chem.* **2008**, *120*, 7159.
(10) Abe, R.; Takami, H.; Murakami, N.; Ohtani, B. *J. Am. Chem. Soc.* **2008**, *130*, 7781.
(11) Liu, J.; Wu, Q.; Ding, Y. *Cryst. Growth Des.* **2005**, *5*, 449.
(12) Zhang, Y.; Chen, Y.; Liu, H.; Zhou, Y.; Li, R.; Cai, M.; Sun, X. *J. Phys. Chem. C* **2009**, *113*, 1750.
(13) Zheng, H.; Sadek, A. Z.; Latham, K.; Kalantar-Zadeh, K. *Electrochem. Commun.* **2009**, *11*, 768.
(14) Tsuchiya, H.; Macak, J. M.; Sieber, I.; Taveira, L.; Ghicov, A.; Sirotna, K.; Schmuki, P. *Electrochem. Commun.* **2005**, *7*, 295–298.
(15) Sadek, A. Z.; Zheng, H.; Breedon, M.; Bansal, V.; Bhargava, S. K.; Latham, K.; Zhu, J.; Yu, L.; Hu, Z.; Spizzirri, P. G.; Wlodarski, W.; Kalantar-zadeh, K. *Langmuir* **2009**, *25*, 9545.
(16) Amano, F.; Li, D.; Ohtani, B. *Chem. Commun.* **2010**, *46*, 2769.
(17) Mukherjee, N.; Paulose, M.; Varghese, O. K.; Mor, G. K.; Grimes, C. A. *J. Mater. Res.* **2003**, *18*, 2296.
(18) Berger, S.; Tsuchiya, H.; Ghicov, A.; Schmuki, P. *Appl. Phys. Lett.* **2006**, *88*, 203119.
(19) Jayatissa, A. H.; Cheng, S. T.; Gupta, T. *J Phys Chem B* **2004**, *109*, 269.
(20) Al Mohammad, A.; Gillet, M. *Thin Solid Films* **2002**, *408*, 302.
(21) Salje, E.; Viswanathan, K. *Acta Crystallogr., Sect. A: Found. Crystallogr.* **1975**, *31*, 356.
(22) Judeinstein, P.; Morineau, R.; Livage, J. *Solid State Ionics* **1992**, *51*, 239.
(23) Pourbaix, M. *Atlas of Electrochemical Equilibria in Aqueous Solutions*; Pergamon Press: Oxford, NY, 1966.
(24) Macak, J. M.; Tsuchiya, H.; Ghicov, A.; Yasuda, K.; Hahn, R.; Bauer, S.; Schmuki, P. *Curr. Opin. Solid State Mater. Sci.* **2007**, *11*, 3.
(25) Paola, A. D.; Quarto, F. D.; Sunseri, C. *Corros. Sci.* **1980**, *20*, 1067.
(26) Lillard, R. S.; Kanner, G. S.; Butt, D. P. *J. Electrochem. Soc.* **1998**, *145*, 2718.
(27) Widenkvist, E.; Quinlan, R. A.; Holloway, B. C.; Grennberg, H.; Jansson, U. *Cryst. Growth Des.* **2008**, *8*, 3753.
(28) Penn, R. L. *J Phys Chem B* **2004**, *108*, 12712.
(29) Chang, L.; Yang, H.; Fu, W.; Yang, N.; Chen, J.; Li, M.; Zou, G.; Li, J. *Mater. Res. Bull.* **2006**, *41*, 1242.
(30) Daniel, M. F.; Desbat, B.; Lassegues, J. C.; Gerand, B.; Figlarz, M. *J. Solid State Chem.* **1987**, *67*, 235.
(31) Tenne, R.; Margulis, L.; Genut, M.; Hodes, G. *Nature* **1992**, *360*, 444.
(32) Teoh, L. G.; Shieh, J.; Lai, W. H.; Hung, I. M.; Hon, M. H. *J. Alloys Compd.* **2005**, *396*, 251.
(33) Ahn, K.; Lee, S.; Dillon, A. C.; Tracy, C. E.; Pitts, R. *J. Appl. Phys.* **2008**, *101*, 093524.
(34) Baserga, A.; Russo, V.; Di Fonzo, F.; Bailini, A.; Cattaneo, D.; Casari, C. S.; Li Bassi, A.; Bottani, C. E. *Thin Solid Films* **2007**, *515*, 6465.
(35) Santato, C.; Odziemkowski, M.; Ulmann, M.; Augustynski, J. *J. Am. Chem. Soc.* **2001**, *123*, 10639.